PAPER

Check for updates

Matching drug and polymer for efficient delivery of anti-inflammatory drugs: PLGA, polyesteramides, and acetalated dextran

Lea C. Klepsch, [ID] [ab] Philipp Dahlke, [ID] [c] Mira Behnke, [ab] Ekaterina Tsarenko, [ab]
Natalie E. Göppert, [ab] Paul Klemm, [ab] Jakob Meyer, [ab] Alan George, [ID] [d]
Mingzhe Chi, [ID] [d] Justyna A. Czaplewska, [ab] Antje Vollrath, [ID] [ab]
Christine Weber, [ID] [ab] Paul M. Jordan, [ID] [bc] Stephanie Schubert, [ID] [ab]
Stephanie Hoeppener, [ID] [ab] Ivo Nischang, [ID] [abef] Marek Sierka, [ID] [bd] Oliver Werz[bc]
and Ulrich S. Schubert [ID] ⋆[abe]

The hydrochalcone derivative **MF-15** and the synthetically derived **BRP-201** are potent anti-inflammatory active pharmaceutical ingredients (APIs) that suffer from poor bioavailability. This necessitates their incorporation into drug delivery systems. To address this limitation, we investigated four polymeric carrier materials. The poly(ester amide)s poly(3-benzylmorpholine-2,5-dione) (**PPheG**) and poly(3-isopropyl-morpholine-2,5-dione) (**PValG**), the benchmark poly(lactic-*co*-glycolic acid) (**PLGA**), and the polysaccharide acetalated dextran (**Ac-Dex**) were used to formulate nanoparticles *via* nanoprecipitation. The nanoparticles had sizes of around 110 to 190 nm with negative zeta potentials. Although atomistic molecular dynamics (MD) simulations predicted enhanced miscibility of **PPheG** and **PValG** with **MF-15**, the highest loading capacity was achieved with **Ac-Dex** (4.2 wt%). None of the **MF-15**-loaded particles elicited a biologic response (*i.e.*, 15-lipoxygenase (LOX)-1 activation) in human M2 monocyte-derived macrophages (MDMs). The consistent failure across all **MF-15** formulations, despite differences in polymer composition, drug loading, and enzymatic degradation profiles, suggests that encapsulation inherently interferes with **MF-15**'s ability to activate 15-LOX-1, irrespective of the carrier system. In contrast, all **BRP-201**-loaded formulations demonstrated potent anti-inflammatory effects in human neutrophils. Overall, our findings demonstrate that polymer–drug miscibility and favorable physicochemical properties alone are insufficient to predict *in vitro* efficacy, highlighting the importance of kinetic and formulation-dependent factors in the successful delivery of anti-inflammatory agents.

1. Introduction

Polymer-based nanoparticles have gained considerable attention as drug delivery systems due to their capability to enhance the bioavailability, stability, and controlled release of active

[a] *Laboratory of Organic and Macromolecular Chemistry (IOMC) Friedrich Schiller University Jena, Humboldtstraße 10, 07743 Jena, Germany.*
E-mail: ulrich.schubert@uni-jena.de

[b] *Jena Center for Soft Matter (JCSM) Friedrich Schiller University Jena, Philosophenweg 7, 07743 Jena, Germany*

[c] *Department of Pharmaceutical/Medicinal Chemistry, Institute of Pharmacy Friedrich Schiller University Jena, Philosophenweg 14, 07743 Jena, Germany*

[d] *Otto Schott Institute of Materials Research (OSIM), Friedrich Schiller University Jena, Löbdergraben 32, 07743 Jena, Germany*

[e] *Helmholtz Institute for Polymers in Energy Applications Jena (HIPOLE Jena), Lessingstraße 12-14, 07743 Jena, Germany*

[f] *Helmholtz-Zentrum Berlin für Materialien und Energie GmbH (HZB), Hahn-Meitner-Platz 1, 14109 Berlin, Germany*

pharmaceutical ingredients (APIs).[1] Among these, poly(lactic-*co*-glycolic acid) (**PLGA**), a polymer approved by the Food and Drug Administration (FDA), has emerged as a widely used biocompatible and biodegradable polymer for nanoparticle formulations.[2,3] Its hydrophobic nature favors the encapsulation of hydrophobic drugs. Its biodegradation ensures a gradual release of the APIs and minimizes the accumulation of the carrier material in the body. Despite these advantages, **PLGA** degradation produces lactic and glycolic acid, which leads to local acidification that can affect the stability of acid-sensitive therapeutics, including certain proteins.[4,5] Although drug encapsulation using **PLGA** can be tailored through the use of materials of different molar masses, end-groups, and lactate to glycolate ratios, it comprises solely ester moieties along the polymer backbone. It is hence reasonable to consider alternative polymer materials for drug encapsulation to increase the structural versatility and enable additional interactions between drug and polymer. Current studies

15516 | *J. Mater. Chem. B*, 2025, **13**, 15516–15529

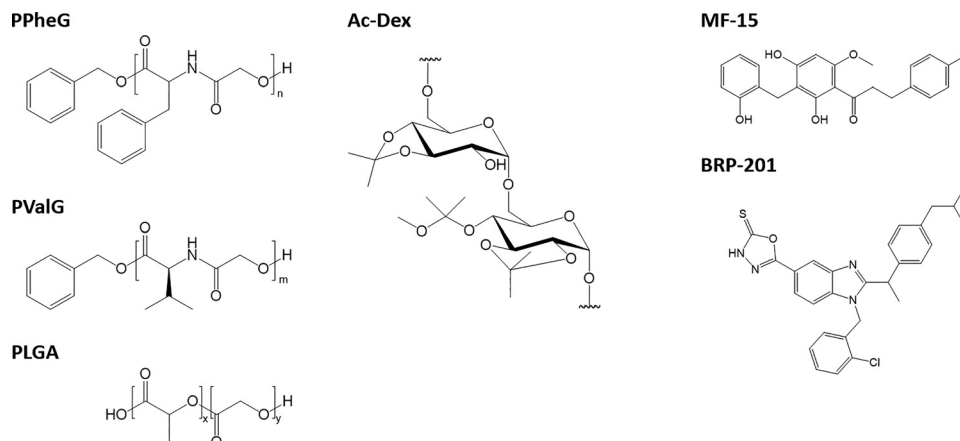This journal is © The Royal Society of Chemistry 2025

Fig. 1 Schematic representation of the structures of the four polymers **PPheG**, **PValG**, **PLGA** (lactide : glycolide 50 : 50, acid terminated) and **Ac-Dex** (degree of substitution (DS) = 2.06, DS cyclic acetal = 1.44, DS acyclic acetal = 0.62) used as carrier materials as well as the two drugs **MF-15** and **BRP-201**.

investigating alternative polymers often exhibit a methodological limitation. Here, single polymer entries are evaluated without comparative analysis across different polymer classes or against the established benchmark **PLGA**. In contrast, we investigated and compared the performance of two poly(ester amide)s (PEA) and an acetalated dextran (Ac-Dex) against **PLGA**, all polymers with distinctly different characteristics in the context of nanocarrier formulation and pharmacological evaluation, for the anti-inflammatory drugs **MF-15** and **BRP-201** that act as lipoxygenase modulator and dual FLAP and mPGES-1 inhibitor, respectively (Fig. 1).[6,7] **BRP-201** has previously been encapsulated by us in several polymer systems,[8] thereby serving as a suitable reference compound for assessing the performance of the tested carriers. In contrast, **MF-15** has, to the best of our knowledge, not yet been encapsulated in polymeric nanoparticles. It was therefore selected as a novel candidate to establish and optimize a formulation protocol for this compound.

PEA feature amide as well as ester moieties, which facilitate hydrogen bonding either between the polymer and the API or among polymers. This might enhance drug encapsulation efficiency through increased molecular interactions between the polymer and the drug. While **PLGA** consists of randomly arranged glycolate and lactate repeating units, PEA can be composed of alternating glycolate and amino acid units.[9] The degradation behavior and other material properties can be tailored by selecting the appropriate amino acid. Several studies have demonstrated the use of PEA for the encapsulation and delivery of various APIs, including proteins (*e.g.* bovine serum albumin),[10,11] genetic material (*e.g.* pDNA),[12,13] and low molar mass drugs (*e.g.* paclitaxel,[14] ibuprofen,[15] doxorubicin[16]).

We selected an L-valine-based PEA (**PValG**), previously identified in our laboratory as a promising drug carrier system,[17] and an L-phenylalanine-based PEA (**PPheG**). The incorporation of the phenyl moiety in **PPheG** may enhance the polymer's hydrophobicity and promote π–π stacking interactions with therapeutic agents featuring aromatic moieties. We hence anticipated a modulated drug encapsulation efficiency and degradation behavior of nanoparticles formulated from **PPheG**.

Ac-Dex was included in this study as a structurally distinct polymer to broaden the comparative analysis of potential carrier matrices beyond polyester-based architectures. Derived from the clinically approved glucose-based polysaccharide dextran,[18] **Ac-Dex** has demonstrated significant potential for various therapeutic applications. Amongst others,[8,19] **Ac-Dex** has been investigated for the encapsulation of various drugs, including **BRP-201**,[20] sorafenib,[21] paclitaxel,[22] and doxorubicin.[23] In addition to its biodegradability, **Ac-Dex** offers several advantageous properties, such as pH sensitivity and the resulting ability to control carrier degradation and release of the API, high drug encapsulation efficiency, as well as excellent biocompatibility.[24]

These promising materials, *i.e.*, **Ac-Dex**, **PValG**, **PPheG**, and the gold standard **PLGA**, were assessed concerning their ability to encapsulate and deliver the two novel anti-inflammatory drugs **MF-15** and **BRP-201** (Fig. 1) into human M2 monocyte-derived macrophages (MDMs) and human neutrophils. In a combined *in silico* and experimental approach, polymer drug interactions were predicted by atomistic molecular dynamics (MD) simulations and probed by high-performance liquid chromatography (HPLC). For the latter, the apparent hydrophobicity of the carrier materials and nanoparticle loading capacities (LC) from dissolved nanoparticle formulations were investigated. Moreover, we assessed stability and enzymatic degradation of nanoparticle suspensions as well as bioactivities.

2. Results and discussion

2.1. High-performance liquid chromatography (HPLC) analysis of carrier materials

The varying overall hydrophobicity of the polymers used may represent a key parameter on the LC values, degradation, and consequently API release. To estimate the apparent hydrophobicity of the polymers, they were investigated by means of liquid chromatography on a hydrophobic, octadecyl- (C18-) modified monolithic silica column with a linear gradient of CH_3CN in the aqueous organic mobile phase. Under such conditions, the polymers are expected to elute according to their overall hydrophobicity.[25,26] As typically observed for

This journal is © The Royal Society of Chemistry 2025

J. Mater. Chem. B, 2025, **13**, 15516–15529 | **15517**
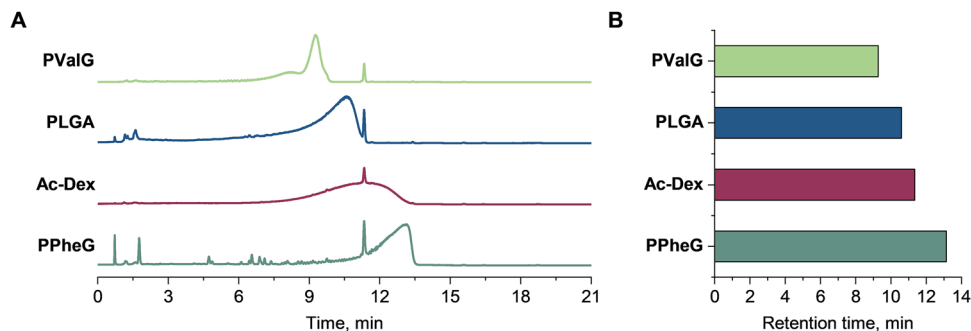
Fig. 2 (A) Overlay of normalized elution traces of polymers recorded by a charged aerosol detector (CAD). (B) Polymer elution times determined as a first moment of the distribution (peak). Conditions: Chromolith® High Resolution RP-18 endcapped column (100 × 4.6 mm), gradient elution programming: the mobile phase composition was kept constant at 50/50 (%, v/v) CH_3CN/H_2O for 1 min, followed by an increase of CH_3CN content to 100% within 10 min and an isocratic hold at 100% CH_3CN for 8 min. Flow rate: 1.0 mL min^{-1}. Column temperature: 30 °C. Injection volume: 5 μL. The polymers were dissolved in 50/50 DMSO/CH_3CN (%, v/v) at a concentration of 1 mg mL^{-1}.

polymers, the elution is governed by slow mass transfer and affected by the dispersity of polymers in terms of molar mass and chemical composition (Fig. 2A). This typically leads to broad elution profiles while both average molar mass and hydrophobicity are expected to correlate with elution time.[27] Fig. 2B reveals **PPheG** appearing to be the most hydrophobic polymer, which is explainable by the benzyl moieties. This is followed by the more hydrophilic polyacetal **AcDex**. Despite its isopropyl substituent, **PValG** eluted earlier than **PLGA**, which comprises methyl substituents on the polymer backbone. Apparently, the amide functionalities render the **PValG** more hydrophilic than the polyester despite its more hydrophobic substituent.

2.2. Molecular dynamics (MD) simulation – Flory–Huggins (FH) interaction parameters χ_I and χ_{II}

In addition to the mere hydrophobicity of the polymers, specific interactions are expected to contribute to the compatibility of carrier materials and APIs. The miscibility of drugs and polymers, estimated *via* FH interaction parameters, was hence objective of atomistic MD simulations. Due to its structure as a statistical copolymer comprising, in theory, twelve differently substituted anhydro-D-glucopyranose repeating units, **Ac-Dex** was excluded from these simulations, as the computational effort required would exceed our available resources.

The FH interaction parameters χ_I and χ_{II} were calculated using two methodologies, identified as methods I and II, which are further described in the experimental section. Shortly, method I is based on differences in Hildebrand solubility parameters δ, which provide a straightforward approach for predicting miscibility in pharmaceutical systems.[28,29] Method II, on the other hand, provides a more comprehensive and precise approach by employing atomistic MD simulations to model polymer–drug mixtures. This technique captures specific intermolecular interactions within binary mixtures, offering a precise representation of the system behavior, in particular for polymer–drug systems. The calculated FH parameters χ_I and χ_{II} (see Section 4.5), along with their corresponding ΔG_{mix}, are presented in Table 1 for both methods. The reliability of this approach has

been previously confirmed through comparisons with experimentally obtained thermodynamic measurements.[30]

The χ_I values for the mixtures of **PLGA**, **PValG**, and **PPheG** with **MF-15** are considered less precise because they are derived from Hildebrand solubility parameters obtained from MD simulations of the pure components. These parameters estimate miscibility without capturing the specific interactions occurring within the mixture.[31] In contrast, the χ_{II} values are derived using cohesive energy densities of the polymer, the API, and their mixture. This allows for a more detailed representation of the interaction behavior between the components, resulting in a better estimation of miscibility. The mixture of **PPheG** with **BRP-201** has a χ_I value of 0.11 and a χ_{II} value of 1.61. A χ value below 0.5 indicates stronger and more favorable interactions between the polymer and the API, while values above 0.5 suggest weaker interactions. The ΔG_{mix} values were negative for all polymer–API mixtures, indicating thermodynamic favorability of each mixture. While the χ_{II} values indicate substantial differences in the interactions across the polymer–drug mixtures, the similar ΔG_{mix} values for the **PValG/MF-15** and **PPheG/MF-15** mixtures suggest that the loading efficiency should remain consistent across investigated systems. The solubility limits of all polymer-**MF-15** mixtures were found to be almost 99%. This means that **MF-15** should be completely miscible with the polymer at all concentrations for all mixtures.

Table 1 Flory–Huggins (FH) parameters χ_I and χ_{II} calculated with methods I and II (see Section 4.5) and the corresponding change in Gibbs free energy of mixing (ΔG_{mix} in J mol^{-1}) for the simulated mixtures of **PLGA**, **PValG** and **PPheG** with **MF-15** and with **BRP-201**. Data for **PValG** with **BRP-201** were taken from Behnke *et al.*[17]

Polymer	API	χ_I	χ_{II}	ΔG_{mix} [J mol^{-1}] (χ_I)	ΔG_{mix} [J mol^{-1}] (χ_{II})
PLGA	**MF-15**	0.02	0.01	−18.4	−18.5
PValG	**MF-15**	0.47	0.49	−30.4	−30.3
PPheG	**MF-15**	0.44	0.75	−31.4	−29.7
PLGA	**BRP-201**	0.00	−0.01	−18.5	−18.5
PValG[17]	**BRP-201**	0.13	3.85	−49.6	−16.1
PPheG	**BRP-201**	0.11	1.61	−49.9	−36.4

15518 | *J. Mater. Chem. B*, 2025, **13**, 15516–15529

This journal is © The Royal Society of Chemistry 2025

In the case of **PLGA** the $\Delta G_{mix}(\chi_{II})$ values for both APIs, **MF-15** and **BRP-201** are identical (-18.5 J mol^{-1}), suggesting comparable but modest miscibility with both drugs. A prior investigation examining a similar **PValG** with the drug **BRP-201** reported a χ_{II} value of 3.85 and a corresponding ΔG_{mix} of -16.1 J mol^{-1}.[17] In comparison, the combination of **MF-15** and **PValG** shows a notably reduced χ_{II} value of 0.49 and a more favorable ΔG_{mix} of -30.3 J mol^{-1}. These results suggest that **MF-15** exhibits an enhanced miscibility and encapsulation capability compared to **BRP-201** for **PValG**. Similarly, the miscibility and thermodynamic behavior of **PPheG** with **MF-15** and **BRP-201** were analyzed here. The mixture of **PPheG** with **MF-15** exhibited a $\Delta G_{mix}(\chi_{II})$ of -29.7 J mol^{-1}, with an enthalpic contribution $\Delta H_{mix}(\chi_{II})$ of 4.1 J mol^{-1} and an entropic contribution $\Delta S_{mix}(\chi_{II})$ of -33.8 J mol^{-1}. For the **PPheG** and **BRP-201** mixture, $\Delta G_{mix}(\chi_{II})$ was found to be -36.4 J mol^{-1}, with $\Delta H_{mix}(\chi_{II})$ of 14.5 J mol^{-1}, corresponding to the high interaction parameter χ_{II} of 1.61, and $\Delta S_{mix}(\chi_{II})$ of -50.9 J mol^{-1}, indicating that entropy significantly contributed to the thermodynamic stability of the **PPheG/BRP-201** mixture. The $\Delta G_{mix}(\chi_{II})$ values for both APIs with **PPheG** were similar, indicating similar miscibility.

2.3. MD simulation – intermolecular hydrogen bonding

Furthermore, intermolecular hydrogen bonding was analyzed by computing the radial distribution function (RDF). The RDF provides insights into hydrogen bonds formed between **MF-15**, **BRP-201** and surrounding polymer chains, indirectly indicating enhanced miscibility and stability of each mixture. Hydrogen atoms covalently bonded to electronegative donor atoms (Dn, typically O or N) and their corresponng acceptor atoms (Ac) were identified within each polymer–API mixture (Fig. 3A–C). Intermolecular Dn–H···Ac interactions (solid lines represent covalent bonds, dotted lines represent hydrogen bonds) were then used to generate RDF plots (Fig. 3D and E), illustrating spatial distribution and strength of hydrogen bonds. In Fig. 3D, the higher RDF peaks for **PValG** and **PPheG** suggest stronger hydrogen bonding interactions with **MF-15**. This correlates with their more negative $\Delta G_{mix}(\chi_{II})$ values (-30.3 and -29.7 J mol^{-1}), indicating greater thermodynamic favorability for hydrogen-bonded structures. Conversely, **PLGA** exhibited significantly lower RDF peaks, corresponding to a less negative $\Delta G_{mix}(\chi_{II})$ value (-18.5 J mol^{-1}), reflecting weaker hydrogen bonding interactions. Therefore, it is predicted, that **PLGA** is less effective at encapsulating **MF-15** due to its weaker hydrogen bonding and lower thermodynamic affinity to the drug. When comparing **MF-15** and **BRP-201**, the RDF plots for **PValG** and **PPheG** show more pronounced peaks for **MF-15**, indicating stronger hydrogen bonding and, thus, more favorable interactions with this drug. In contrast, **PLGA** exhibits similarly low and nearly identical peak intensities for both APIs, suggesting limited hydrogen bonding interactions with **MF-15** and **BRP-201**. For **BRP-201**, however, **PPheG** displays the most favorable $\Delta G_{mix}(\chi_{II})$ value despite lower hydrogen bonding RDF peak intensity, indicating that additional non-hydrogen-bonding
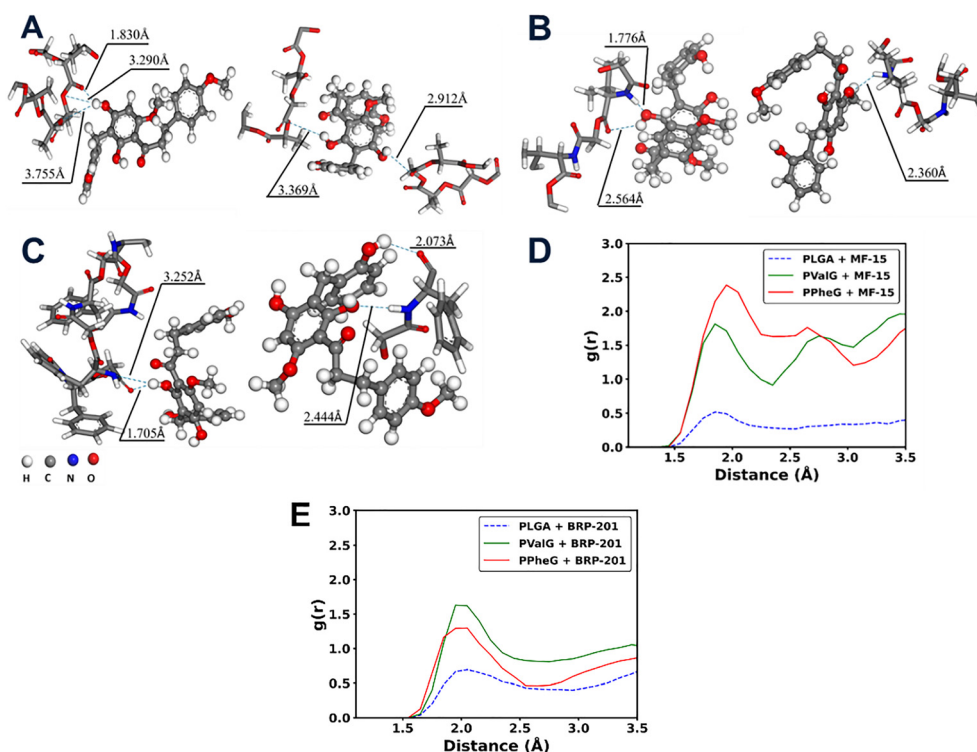

Fig. 3 Ball-and-stick representation of examples of polymer segment – API interactions (A)–(C), with (A) **PLGA** with **MF-15**, (B) **PValG** with **MF-15** and (C) **PPheG** with **MF-15**. (D) RDF plot for intermolecular hydrogen bonding interactions between **MF-15** and the polymers. (E) RDF plot for intermolecular hydrogen bonding interactions between **BRP-201** and the polymers.

This journal is © The Royal Society of Chemistry 2025

J. Mater. Chem. B, 2025, **13**, 15516–15529 | **15519**

interactions and entropic contributions also play a decisive role in stabilizing this mixture.

2.4. Formulation and characterization of the particles

The nanoprecipitation formulation protocol for the four polymers with the two APIs was adapted from Behnke *et al.*[17] and optimized for the **MF-15** encapsulation. The optimization involved increasing the polymer concentration to 15 mg mL^{-1} and the drug feed to 5 wt% relative to the polymer (SI Table S1). Acetone was used as solvent for **PValG**, **PLGA**, and **Ac-Dex** and replaced tetrahydrofuran, a class 2 solvent that should be minimized in formulations due to its toxicity.[32] Due to the limited solubility of **PPheG** in acetone, dimethyl sulfoxide (DMSO) was used as an alternative. Acetone and DMSO are class 3 solvents, which are preferred for pharmaceutical formulations due to their lower toxicity and reduced risk than class 2 solvents.[32] Similarly, **BRP-201**-loaded nanoparticles were prepared using the same solvents and an initial drug feed of 5 wt%. To counteract the tendency of **BRP-201** loading to produce larger particle sizes compared to the encapsulation of **MF-15**, the polymer concentration was decreased to 10 mg mL^{-1}. By lowering the polymer concentration, particle sizes were consistently maintained below 200 nm. This adjustment takes advantage of the empirical observation that lower polymer concentration leads to smaller nanoparticle sizes.[33] The size range (<200 nm) was deliberately chosen, as nanoparticle dimensions are a pivotal factor influencing cellular uptake pathways and overall bioavailability.[34]

The resulting formulations comprised twelve different particle types: Four blank particle batches, four particles loaded with **MF-15** and four particles loaded with **BRP-201** (SI Table S2). Each formulation was thoroughly characterized for key properties, including hydrodynamic diameter (d_{h}), polydispersity index (PDI), zeta potential (ζ), particle concentration, LC, and encapsulation efficiency (EE). Additionally, the polyvinyl alcohol (PVA) content, overall yield, resuspension behavior (SI Table S3), and stability were assessed, alongside with particle degradation in the presence of proteinase K. Furthermore, biocompatibility and API delivery performance were extensively evaluated.

The unloaded particles exhibited d_{h} values between 110 and 184 nm (0.03 < PDI < 0.11), as determined by DLS (Fig. 4). Intensity plots of hydrodynamic diameters from DLS measurements are provided in Fig. S4 to S6. Overall, drug encapsulation within the polymer carriers led to a slight increase in apparent particle size, especially for **BRP-201**, despite a lower polymer concentration used during nanoprecipitation. The ζ-potential of all particles was negative, suggesting sufficient repulsion between particles and colloidal stability of the nanoformulations (-32 mV < ζ < -16 mV; SI Table S2).

SEM was conducted as a crucial quality control measure to visualize the nanoparticles, verify the sizes obtained from DLS, and, most importantly, assess the absence of free API precipitates in the formulations (Fig. 4D). The analysis revealed well-defined, spherical particles with sizes similar to those determined by DLS. For all **MF-15** formulations, no free drug precipitates were found. However, in case of **BRP-201**, some
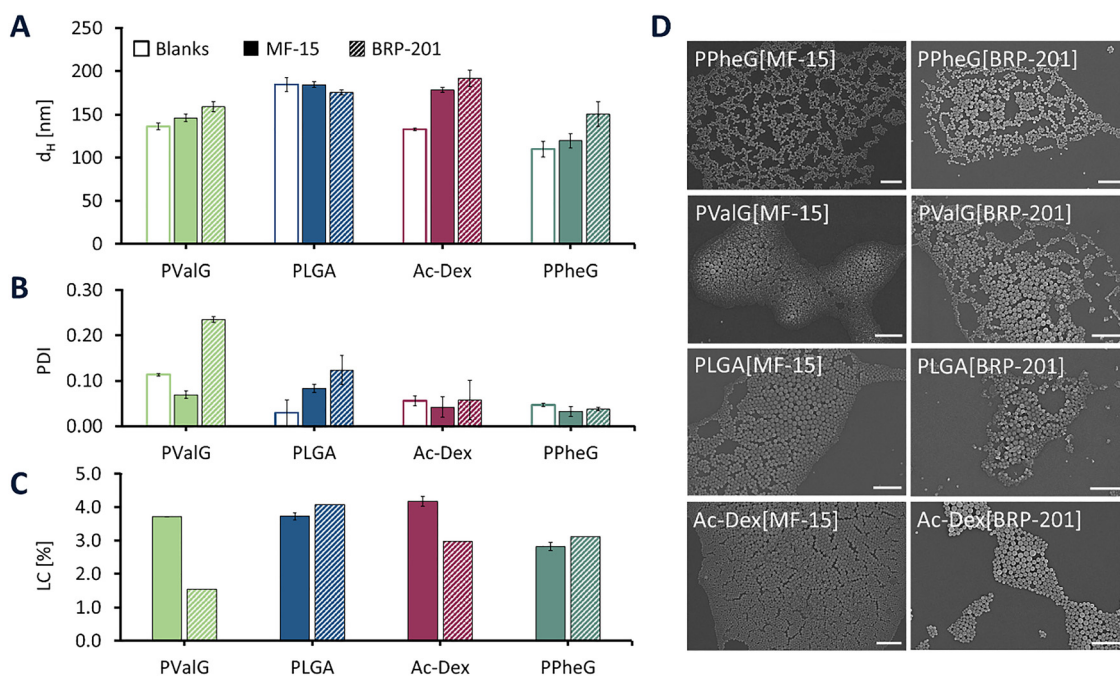

Fig. 4 Particle characteristics of unloaded, **MF-15** loaded, and **BRP-201** loaded particles prepared from **PValG** (light green), **PLGA** (blue), **Ac-Dex** (purple) and **PPheG** (turquoise). (A) z-average hydrodynamic diameter (d_{h}) of purified particles. (B) Polydispersity index (PDI) obtained by DLS. (C) Loading capacity (LC) values of particles for **MF-15** (n = 3) and **BRP-201** (n = 2) determined by HPLC (small error bar for **PPheG[MF-15]** not visible). (D) SEM images of drug loaded particles after purification (scale bar: 1 μm).

15520 | *J. Mater. Chem. B*, 2025, **13**, 15516–15529

This journal is © The Royal Society of Chemistry 2025

precipitates were visible, particularly in the **PValG[BRP-201]** formulation (Fig. S7). This system also exhibited a higher PDI value of 0.23, whereas all other formulations had PDI values below 0.12 with one major population (size distributions are shown in Fig. S5 to S6). The presence of free **BRP-201** precipitates could explain the increased PDI value observed for **PValG[BRP-201]**. Larger drug aggregates are indicated in intensity based DLS data which are absent after additional purification (see size distributions in Fig. S8). These findings suggest that a 5 wt% drug feed was excessive for this formulation, leading to incomplete drug entrapment within the polymer matrix.

2.5. Determination of drug loading: experiment and *in silico*

The drug loading of all **MF-15** and **BRP-201** formulations was determined using liquid chromatography. The lyophilized samples were dissolved and the drug content was determined according to a previously developed protocol (Fig. S11 and Fig. S12).[35] In case of **MF-15**-loaded particles, the elution patterns were only monitored by diode array detection (DAD) due to the presence of phosphoric acid in the eluent. The elugrams of **BRP-201**-loaded nanoparticles were recorded by charged aerosol detection (CAD) as well as DAD (Fig. S12). Calibration curves for **BRP-201** and **MF-15** were established using a series of diluted stock solutions measured under the same elution conditions as for the particle samples (Fig. S13). The mean LC values were determined based on two repetitive formulations containing **BRP-201** (Fig. S14 to S17) and three repetitive formulations containing **MF-15** (Fig. S11). Based on the liquid chromatography data, LC and EE values were calculated (Table S2). The LC values are discussed under the condition that the attempted drug load was kept constant at 5 wt%.

All carrier systems were able to encapsulate both APIs in sufficient quantities (LC_{MF-15} = 2.82% to 4.18% and $LC_{BRP-201}$ = 1.53 to 4.08%, Fig. 4C and Table S2). **PValG** and **Ac-Dex** were able to encapsulate larger amounts of **MF-15** than **BRP-201**. This agrees with the MD simulations, which predicted an enhanced miscibility of **MF-15** and **PValG**. Similar LC values for both APIs were observed for **PPheG** and **PLGA**, which is also in accordance with the *in silico* results of **PPheG**.

Among all polymers investigated, **Ac-Dex** featured the highest LC value for **MF-15**. The LC values of **PValG** and **PLGA** were very similar, whereas the use of **PPheG** resulted in the lowest LC value. This is in disagreement with the *in silico* studies, which predicted unlimited solubility for all polymer–**MF-15** mixtures analyzed. These findings demonstrate that thermodynamic compatibility is not the sole factor determining LC in nanoparticulate formulations; kinetic effects may also play a significant role. However, the FH interaction parameter ($\chi_{II} > 0.5$) indicated a weaker interaction of **MF-15** with **PPheG** than with **PValG** and **PLGA**. The LC value for **BRP-201** and **PValG** was in line with the miscibility limit of 1.5 wt%.[17] **Ac-Dex** and **PPheG** were able to encapsulate 3 wt% of the drug. The highest LC value for **BRP-201** was achieved with **PLGA**, exceeding the previously obtained value of 2.1 wt%.[17] Notably, no clear correlation was observed between the hydrophobicity of the polymers and their loading capacity for either drug, suggesting

that specific interactions between the polymers and the active ingredients play a more decisive role. In combination with SEM analysis, the results demonstrate that all carriers except **PValG** successfully encapsulated **BRP-201** at an initial drug load of 5 wt%. Similarly, at the same initial loading, **MF-15** was effectively encapsulated by all polymers.

2.6. Nanoparticle stability and degradation studies

The stability of all formulations was evaluated over time. Further experiments were performed after lyophilization and resuspension as key factors determining the stability of drug carrier systems.[36] It is well established that freeze-drying and subsequent reconstitution is one of the most critical steps for many API formulations.[37] Encapsulation of both APIs had no adverse effects on the stability of the formulations after purification. However, stability issues became evident upon resuspension of the lyophilized samples (Table S3). In particular, the **PValG** and **PPheG** formulations were more cumbersome to resuspend. The addition of small amounts of 3% (w/v) aqueous PVA solution before freeze-drying enable better resuspensibility of drug-loaded **PValG** particles (Fig. S9). In contrast, the **PPheG** formulation continued to show larger sizes after lyophilization and resuspension (Fig. S10).

While stability is a crucial factor for nanoparticle formulations, it is equally important that the particles degrade within a suitable timeframe, releasing the encapsulated API without leading to carrier material accumulation.[38] The degradation process primarily depends on the degradability of the polymer, although particle properties, such as size and the associated volume-to-surface area ratio, also play a significant role.[17] One common approach to study the degradation of polymer-based nanoparticles involves the use of enzymes such as esterases, lipases, or proteases.[39,40] Here, proteinase *K* was selected due to its broad substrate specificity.[41] To assess degradation, all nanoparticles were incubated with a proteinase *K* solution at a fixed nanoparticle-to-enzyme mass ratio of 1:25. DLS was employed to monitor changes in count rate and particle size over time, with detector settings kept constant (Fig. 5).

The apparent t_{50} value, *i.e.* the value at which half of the initial count rate was reached, was used to compare the enzymatic degradation behavior of the different carriers. **PLGA** and **PValG** exhibited similar count rate trends with apparent t_{50} values below 20 min. The degradation of **PPheG** proceeded slower, which is in line with its increased hydrophobicity. The steric demand of the benzyl substituent at the phenyl alanine units could also hinder accessibility for the enzyme. The **Ac-Dex** nanoparticles revealed the slowest degradation. This is likely because **Ac-Dex** does not feature any ester or amide moieties, whose hydrolysis would be catalyzed by the enzyme (a proteinase). However, it was shown that **Ac-Dex** degrades efficiently in acidic environments, which are typical for inflammatory conditions.[20] Fig. 5B presents the particle size as a function of time during the degradation process. The apparent particle size remained invariant, or showed a decrease in instances, when the count rate approached zero. Following that, an increase in apparent particle size was observed in most instances, which
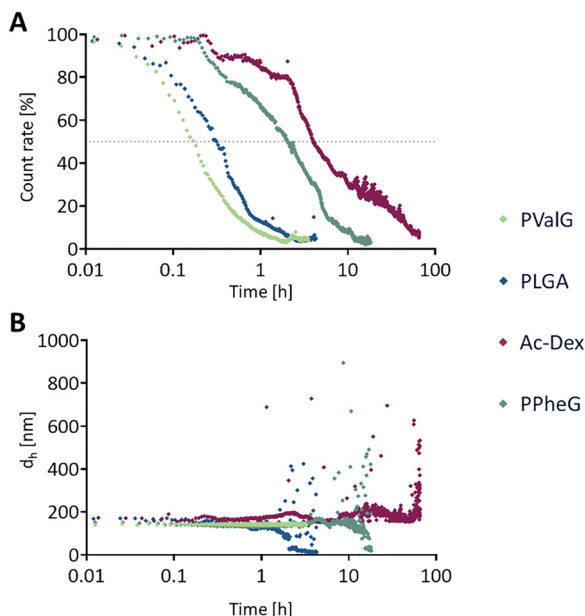
This journal is © The Royal Society of Chemistry 2025

J. Mater. Chem. B, 2025, **13**, 15516–15529 | 15521

Fig. 5 Degradation of nanoparticles in the presence of proteinase K as monitored by DLS. The respective mass ratio used was 1 : 25 (nanoparticle : enzyme). (A) Semi-logarithmic plot of count rate over time with the horizontal dotted line as a guide to the eye, indicating a 50% decrease in count rate. (B) Semi-logarithmic plot of z-average hydrodynamic diameter (d_h) over time.

can be attributed to the remaining presence of material aggregates in solution. Overall, while each polymer carrier exhibited a distinct degradation profile, all demonstrated effective enzymatic breakdown in the presence of proteinase K. These findings suggest that the nanoparticles are capable of releasing their cargo in cellular environments, potentially though enzymatic or other biologically mediated degradation pathways.

2.7. Pharmacological evaluation of the API (MF-15 or BRP-201) loaded nanoparticles

All loaded particles were subsequently examined for their pharmacological activity, applying the same concentration of free and encapsulated drug. To assure that the carriers are appropriate as delivery systems for drugs in general, we tested **BRP-201**, a potent inhibitor of 5-LOX activating protein (FLAP), when encapsulated in nanoparticles.[42] We utilized human neutrophils, which express high levels of 5-LOX and FLAP, to metabolize arachidonic acid into pro-inflammatory leukotrienes upon stimulation.[43] **BRP-201** encapsulated into the four carrier materials (0.3 μM final concentration) led to potent inhibition of FLAP decreasing 5-LOX product formation in neutrophils across all carrier systems, with significance particularly evident for **PValG** (Fig. 6A). The findings presented here confirm the suitability of all carrier materials as effective nanoparticle drug delivery systems. Additionally, they also support the results from our previous study on the use of **PValG** for the delivery of **BRP-201**.[17]

Likewise, the biological activity of **MF-15** loaded nanoparticles is crucial for their suitability as an anti-inflammatory treatment,

in particular since **MF-15** has not previously been investigated in encapsulated form using polymer-based carriers. **MF-15** is a potent activator of 15-LOX-1, the key enzyme for the biosynthesis of specialized pro-resolving mediators (SPMs) and lipoxins *via* stereoselective oxygenation of polyunsaturated fatty acids (PUFAs) like arachidonic acid (AA), docosahexaenoic acid (DHA) or eicosapentaenoic acid (EPA).[44] 15-Hydroxyeicosatetraenoic acid (15-HETE) derived from AA, 17-hydroxydocosahexaenoic acid (17-HDHA) derived from DHA and 15-hydroxyeicosapentaenoic acid (15-HEPE) derived from EPA are 15-LOX-derived precursors for lipoxins and SPMs like resolving D5 (RvD5) or RvE4, respectively.[45] We chose human M2-MDMs as 15-LOX-1-rich innate immune cells to test the biological activity of **MF-15**-loaded particles. Previous studies showed that both **MF-15** and **BRP-201** exhibit consistent biological activities in such MDM incubations without any loss of activity due to instability.[6,7] After incubation of the M2-MDMs with **MF-15**-loaded particles for 180 min, corresponding to a concentration of 3 μM **MF-15**, only weak and non-significant increases of 15-LOX product formation were observed. This contrasts the strong up-regulatory effect of free **MF-15** (3 μM) in the same setting (Fig. 6C). None of the blank or **MF-15**-loaded nanoparticles displayed detrimental effects on membrane integrity as studied by an LDH release assay (Fig. 6B). Altogether, these data show that encapsulation of **MF-15** abolishes its induction of 15-LOX-1 product formation, suggesting that these **MF-15**-loaded nanoparticles are unsuitable as a pharmaceutical formulation. Up to now it is not fully understood why the free API is effective, but not the encapsulated one. It remains to be seen whether this effect occurs in other particle systems. Since the activation mechanism, and particularly the activation kinetics, of 15-LOX-1 is unclear, the kinetic requirements of drug release from nanoparticles to achieve the activation of 15-LOX-1 can only be speculated. Furthermore, it is possible that the subcellular localization inside the cell where the degradation and release of **MF-15** occurs is relevant for 15-LOX-1 activation, and the free drug needs to accumulate at different organelles than those that **MF-15** encounters when it is released from particles. It is assumed that **MF-15** requires a high initial concentration to produce a noticeable effect; however, in the encapsulated form, release of the API is rather slow and occurs over a specific timescale, which may not allow the required dose to be achieved. Faster degrading particles, on the contrary, may release the drug too early, leading to crushing out and subsequently causing undesired opsonization and rapid clearance from the body. A novel pro-drug approach for **MF-15**, where the API is not encapsulated into particles, may be more promising.

3. Conclusion and outlook

This study highlights the complex interplay between polymer composition, drug properties, and formulation parameters of drug-loaded nanoparticles for the design as effective drug delivery systems. The four investigated polymers, *i.e.*, two PEAs (**PPheG** and **PValG**), **PLGA**, and **Ac-Dex**, were successfully formulated into nanoparticles with low PDI values and were able
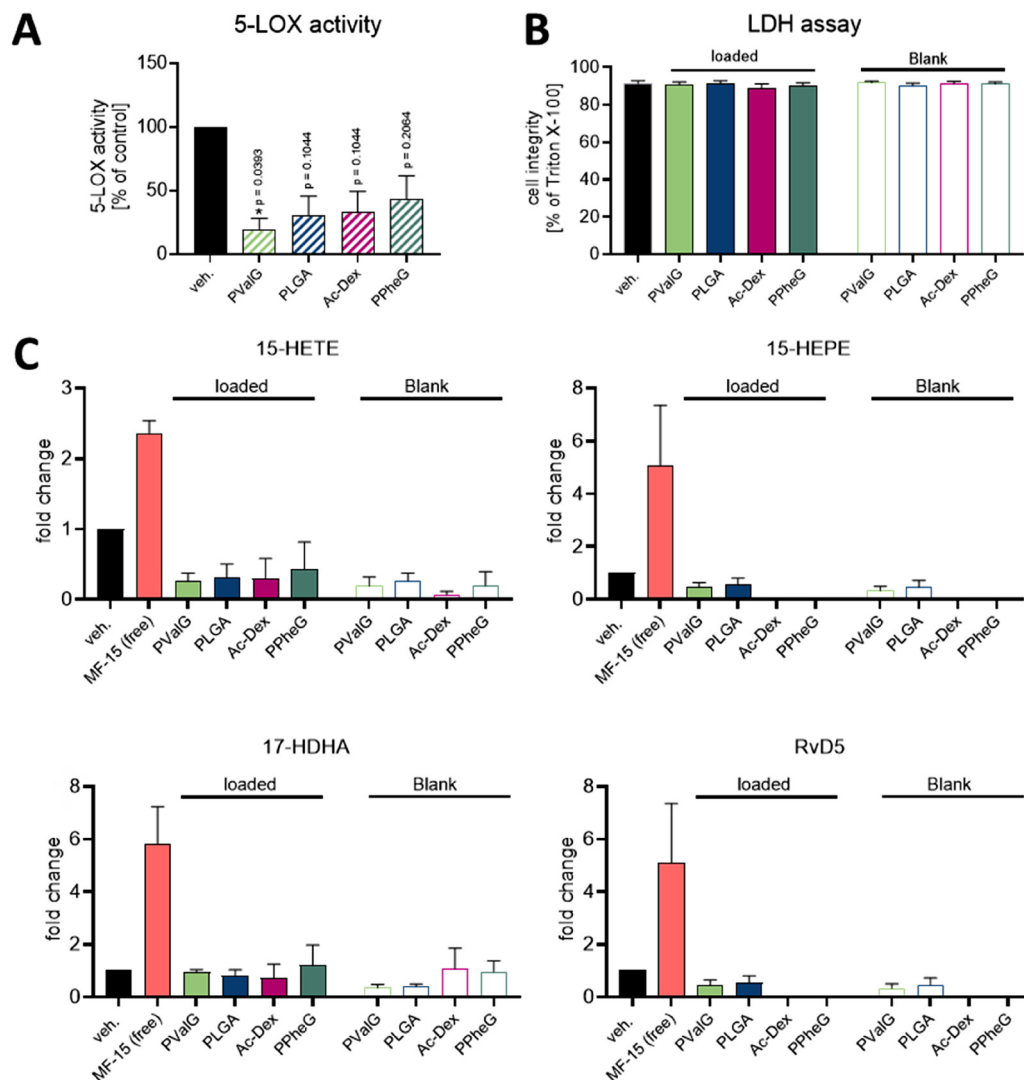
15522 | *J. Mater. Chem. B*, 2025, **13**, 15516–15529

This journal is © The Royal Society of Chemistry 2025

Fig. 6 Biological effects of drug-loaded nanoparticles on lipid mediator formation. (A) 5×10^6 neutrophils were preincubated with PBS or nanoparticles with **BRP-201** (0.3 μM) for 15 min and then stimulated with 2.5 μM A23187 for 10 min. Values are given as 5-LOX products (LTB$_4$, *trans*-LTB$_4$, *epi-trans*-LTB$_4$, and 5-HETE) in percentage of control. (B) 1×10^6 M2-like MDMs were incubated with PBS, nanoparticles with or without **MF-15** for 180 min and the release of LDH was assessed. Data are shown as % of positive control. (C) 1×10^6 Mio M2-like MDMs were incubated with PBS (vehicle), free **MF-15** (3 μM), nanoparticles with or without **MF-15** (corresponding to 3 μM **MF-15** in the incubation) for 180 min. Lipid mediators (15-HETE, 15-HEPE, 17-HDHA, RvD5) are shown as fold change *versus* vehicle control. For statistical analysis matched one-way ANOVA with Tukey's multiple comparisons test was used; * $p < 0.05$.

to encapsulate the anti-inflammatory APIs **MF-15** and **BRP-201**. The resulting particles exhibited high post-purification stability during storage, and demonstrated enzyme-responsive degradability in the presence of proteinase *K*. While MD simulations provided valuable insights into the thermodynamic compatibility of the polymers with **MF-15** and **BRP-201**, they alone proved insufficient to predict loading capacity and delivery performance of the carriers. Additional factors, such as formulation conditions and kinetic requirements of API release from nanoparticles to reach an activation of the 15-LOX-1 also exert crucial impact on the overall carrier performance. This was demonstrated by the obtained *in vitro* pharmacological evaluations of the various loaded particles.

Although all API-loaded nanoparticles exhibited desirable properties regardless of the polymer or drug used, pharmacological evaluation revealed a marked contrast in outcomes. While all **BRP-201**-loaded formulations demonstrated a clear anti-inflammatory effect, none of the **MF-15**-loaded particles elicited a biologic response. The consistent failure across all **MF-15** formulations, despite differences in polymer composition, drug loading, and degradation profiles, suggests that encapsulation inherently interferes with **MF-15**'s ability to activate 15-LOX-1, irrespective of the carrier system. It is hypothesized that the kinetic conditions required for an effective drug release, namely an initial burst to rapidly reach effective concentrations for 15-LOX-1 activation are not met by these nanoparticle systems. As a potential alternative, a strategy involving covalent conjugation of **MF-15** to hydrophilic polymers, such as PEG or hydrophilic poly(2-oxazoline)s, may overcome these limitations and will be explored in future studies.

4. Materials and methods

4.1. Materials

Purified water was obtained from a GenPure ultrapure water purification system (Thermo Scientific) and was used in all stages of nanoparticle preparation, purification, and characterization studies. HPLC grade acetonitrile and water were purchased from VWR. The *ortho*-phosphoric acid (85%) for HPLC and the iodine–potassium iodide solution (according to Lugol for the PVA assay) were purchased from Merck. The Resomer RG 502 H (**PLGA**, M_w 7000 to 17 000 g mol^{-1}, lactide : glycolide 50 : 50, acid terminated), poly(vinyl alcohol) (PVA) (Mowiol 4-88, M_w 31 000 g mol^{-1}), proteinase *K* from *Tritirachium* and dimethylsulfoxide (DMSO, anhydrous $\geq$ 99.9%) were obtained from Sigma-Aldrich. Acetone (99 + %, extra pure) was purchased from Acros Organics was received from Carl Roth GmbH. Triethylamine (Et$_3$N, 99%) was obtained from Thermo Scientific.

BRP-201[46] and **MF-15**[44] were synthesized based on established procedures.

The syntheses of **Ac-Dex**, **PValG**, and **PPheG** are described in the SI.

4.2. Nanoprecipitation of blank and MF-15 loaded nanoparticles

PLGA, **Ac-Dex** or **PValG** (15 mg) were dissolved in acetone (1 mL). **PPheG** (15 mg) was dissolved in DMSO (1 mL). **MF-15** was dissolved in DMSO with a concentration of 10 mg mL^{-1}. For the drug loaded particles, the polymer solution was mixed with 75 μL of the **MF-15** stock solution. In a glass vial, 8 mL of 0.3% (w/v) aqueous PVA solution were prepared. For formulations involving **Ac-Dex**, 50 μL of a 0.01% (v/v) TEA solution was added. The polymer/drug solutions were transferred to a 2 mL syringe with a 21Gx4$^{3/4}$ (0.8 × 120 mm) cannula, which was mounted on the syringe pump (Aladdin AL1000-220, World Precision Instruments). The cannula was bent in a 90° angle and placed in the glass vial, touching the glass wall. The polymer solution was infused into the aqueous phase at a flow rate of 2 mL min^{-1}, while the solution was stirred at 800 rpm. The resulting solution was stirred at 800 rpm under the fume hood overnight. The following day, nanoparticle purification was carried out *via* centrifugation at 11 000 rpm for 60 minutes at 20 °C using a 5804 R centrifuge (Eppendorf). After centrifugation, the supernatant was carefully discarded, and the pellet was resuspended in water (2 mL, **Ac-Dex** 40 μL 0,01% (v/v) TEA solution was added). The dispersions were first vortexed, followed by sonication in an ultrasonic bath for 30 minutes, and then stored overnight at 4 °C to allow the particle suspension to equilibrate. For subsequent analyses, aliquots of the dispersion were freeze-dried using a Christ Alpha 2–4 LD plus lyophilizer. The nanoparticle mass was measured with a MYA 11.4Y microbalance (Radwag Waagen), and the final concentration was determined by dividing the mass of the lyophilized material by the volume initially subjected to lyophilization.

4.3. Nanoprecipitation of BRP-201 loaded nanoparticles

PLGA, **Ac-Dex** or **PValG** (10 mg) were dissolved in acetone (1 mL). **PPheG** (10 mg) was dissolved in DMSO (1 mL).

BRP-201 was dissolved in DMSO with a concentration of 10 mg mL^{-1}. The polymer solution was mixed with 50 μL of the **BRP-201** stock solution. In a 20 mL glass vial, 8 mL of 0.3% (w/v) aqueous PVA were prepared. For formulations involving **Ac-Dex**, 800 μL of a 0.1% (v/v) TEA solution was added. The polymer/drug solutions were transferred to a 2 mL syringe with a 21Gx4$^{3/4}$ (0.8 × 120 mm) cannula, which was mounted on the syringe pump (Aladdin AL1000-220, World Precision Instruments). The cannula was bent to a 90° angle and placed in the aqueous solution, touching the glass wall. The polymer solution was infused into the aqueous phase at a flow rate of 2 mL min^{-1}, while the solution was stirred at 800 rpm. The resulting solution was stirred at 800 rpm under the fume hood overnight. The following day, nanoparticle purification was carried out *via* centrifugation at 11 000 rpm for 60 minutes at 20 °C using a 5804 R centrifuge (Eppendorf). After centrifugation, the supernatant was carefully discarded, and the pellet was resuspended in water (2 mL, **Ac-Dex** 2 mL of 0.01% TEA solution was used). The dispersions were first vortexed, followed by sonication in an ultrasonic bath for 30 minutes, and then stored overnight at 4 °C to allow the particle suspension to equilibrate. For subsequent analyses, aliquots of the dispersion were freeze-dried using a Christ Alpha 2–4 LD plus lyophilizer. The nanoparticle mass was measured with a MYA 11.4Y microbalance (Radwag Waagen), and the final concentration was determined by dividing the mass of the lyophilized material by the volume initially subjected to lyophilization.

4.4. Molecular dynamics simulation – computational details

Molecular dynamics (MD) simulations were conducted using the Materials Studio (Version 2022)[47] simulation platform alongside the COMPASS III force field, following the workflow established in previous studies.[30,48] All MD simulations were carried out with the Forcite module in Materials Studio. Compounds were modeled as three-dimensional periodic amorphous cells constructed through a configurational bias Monte Carlo procedure within the Amorphous Cell module, based on algorithms developed by Theodorou and Suter.[49]

The simulation cells for pure **PLGA** consisted of five polymer chains, each containing 184 repeating units. Similarly, cells for **PValG** and **PPheG** included five polymer chains with 93 and 90 repeating units, respectively. For the API, **MF-15**, the unit cell contained 100 molecules. 12 random initial structures were generated for pure **PLGA** and **PValG**, and 13 for **PPheG**. Similarly, 13 initial structures were created for the API model, and ten configurations were generated for each mixture model. For the simulations of **PPheG** with **BRP-201**, all unit cells of pure **PPheG** contained 10 polymer chains and a total of 550 repeating units. The unit cell of **BRP-201** contained 100 molecules, while the unit cells of **PPheG** and **BRP-201** mixture models comprised five polymer chains and one drug molecule. 12 random initial structures were generated for pure **PPheG**, **BRP-201**, and ten configurations were generated for each **PPheG-BRP-201** mixture model. These initial structures underwent geometric optimization, followed by refinement with MD simulations combined with a simulated annealing process to yield more energetically stable configurations.

15524 | *J. Mater. Chem. B*, 2025, **13**, 15516–15529

This journal is © The Royal Society of Chemistry 2025

All simulations used a time step of 1 fs and applied the Nosè–Hoover thermostat.[50,51] During simulated annealing, structural models were equilibrated at 300 K within a canonical (NVT) ensemble, with temperatures subsequently increased in 100 K increments to reach 1000 K over seven steps. The temperature was then decreased back to 300 K in 100 K increments, equilibrating each step for 10 ps.

Following this, MD simulations were performed within an isothermal–isobaric (NPT) ensemble at a target pressure of zero and temperature of 300 K. The simulations began with a 100 ps equilibration period, using a Berendsen barostat,[52] followed by a 300 ps simulation using a Parrinello–Rahman barostat.[53] Average cell parameters of the structural models were evaluated from the final 200 ps of the NPT simulations. The unit cells of the final NPT structures were scaled to the average cell parameters and equilibrated for an additional 250 ps using the NVT ensemble at 300 K. Average values of properties were subsequently calculated from 200 ps of additional NVT simulations.

4.5. Calculations of the Gibbs free energy of mixing - computational details

Based on the lattice model, Flory–Huggins (FH) theory[54,55] describes the mixing behavior of binary systems through a combination of enthalpic and entropic contributions.[56] This approach allows for straightforward calculations of the Gibbs free energy of mixing[57,58]

$$\Delta G_{\text{mix}} = RT\left[\frac{\phi_{\text{p}}}{x_{\text{p}}}\ln\phi_{\text{p}} + \phi_{\text{d}}\ln\phi_{\text{d}} + \phi_{\text{p}}\phi_{\text{d}}\chi\right] \qquad (1)$$

where R is the gas constant, T denotes the temperature, ϕ_{p} and ϕ_{d} are the volume fractions of the polymer and drug respectively, x_{p} represents the degree of polymerization of the polymer, and χ is the FH interaction parameter. The first two terms represent the combinatorial entropy contributions, while the third term reflects enthalpic contribution.[59]

The FH interaction parameter χ can be calculated using two methodologies, identified as methods I and II. Method I is based on differences in Hildebrand solubility parameters δ, which provide a straightforward approach for predicting miscibility in pharmaceutical systems.[28,29] Here, χ is calculated based on the Hildebrand solubility parameters of pure substances as[60]

$$\chi_{\text{I}} = \frac{V_{\text{m}}}{RT}(\delta_{\text{p}} - \delta_{\text{d}})^2, \qquad (2)$$

where V_{m} is the molar volume of the lattice segment in FH theory, approximated here as the molar volume of each chain unit or API, and δ_{p} and δ_{d} are the Hildebrand solubility parameters of the polymer and drug, respectively. δ is defined as the square root of cohesive energy density CED,[61]

$$\delta = \sqrt{\text{CED}} = \sqrt{\frac{\Delta H_{\text{vap}} - RT}{V_{\text{m}}}} \qquad (3)$$

where ΔH_{vap} is the heat of vaporization or enthalpy of vaporization.

Method II provides a more comprehensive and precise approach by employing atomistic MD simulations to model polymer–drug mixtures. This technique captures specific intermolecular interactions within binary mixtures, offering a precise representation of the system behavior, especially for complex systems. In this approach, the FH parameter is defined as[17]

$$\chi_{\text{II}} = \frac{V_{\text{m}}}{RT}\left(\phi_{\text{p}}\text{CED}_{\text{p}} + \phi_{\text{d}}\text{CED}_{\text{d}} - \text{CED}_{\text{p}-\text{d}}\right), \qquad (4)$$

where CED_{p} and CED_{d} are the cohesive energy densities of the polymer and API, respectively, and $\text{CED}_{\text{p}-\text{d}}$ is the cohesive energy density of the polymer–drug mixture.

4.6. Dynamic light scattering (DLS) and electrophoretic light scattering (ELS)

DLS and ELS were employed to analyze the nanoparticle populations in terms of size, distribution of sizes, and zeta potentials (ζ) using a Zetasizer Ultra (Malvern Panalytical GmbH, United Kingdom). The Zetasizer utilizes a 633 nm wavelength laser. Measurements were performed in polystyrene microcuvettes (Brand GmbH + Co KG, Germany) at 25 °C while the intensity fluctuations were recorded at a back-scattering angle of 174.7°. The z-average hydrodynamic diameter (d_{h}) and polydispersity index (PDI) of the particles were used to judge on nanoparticle quality. d_{h} and PDI were assessed at three stages: (i) Post-evaporation of the organic solvent, (ii) after centrifugation and resuspension in water, and (iii) after lyophilization and resuspension in water. The zeta potential was measured post-centrifugation and resuspension in water using a DTS1070 capillary cuvette. For both types of measurements, the nanoparticles were diluted 1:100 in pure water and measured five times for d_{h} and PDI, with 15 runs each lasting 1.68 seconds, and three times for ZP determination. The data is reported as average and standard deviation among all repeated formulations.

DLS measurements for assessing particle stability post-freeze-drying were performed using the same protocol. Freeze-dried particles were resuspended in purified water and allowed to equilibrate overnight in the fridge at 4 °C. The following day, the resuspended nanoparticles were diluted 1:10 with purified water before characterization.

4.7. Nanoparticle degradation studies with proteinase K

The degradation behavior of the nanoparticles was investigated by DLS measurements according to a previously published procedure.[17] For this purpose, nanoparticles in suspension were incubated with a proteinase K solution (2 mg mL^{-1} in water) at 37 °C in a mass ratio of 1:25 (particles:proteinase K). The mean count rate was used as a readout (at a fixed attenuator of 8) and the initially measured count rate was set equal to 100%. Consequently, the count rate trend over time is represented in values %.

4.8. Scanning electron microscopy (SEM)

A Sigma VP field emission SEM (Carl-Zeiss AG, Germany) was used to image the nanoparticles. Micrographs were acquired with the InLens detector at an acceleration voltage of 6 kV.

This journal is © The Royal Society of Chemistry 2025

J. Mater. Chem. B, 2025, **13**, 15516–15529 | **15525**

Nanoparticle formulations were initially diluted with water in a 1:9 ratio. 7 μL was pipetted onto mica substrates and air dried. Prior to the measurements, the samples were coated with a thin layer of platinum (4 nm) using sputter coating (CCU-010 HV, Safematic GmbH, Switzerland).[17]

4.9. PVA-assay

The amount of PVA (%, w/w) in the freeze-dried nanoparticles was quantified using UV-vis spectroscopy (at 690 nm) after forming a PVA–iodine complex using iodine-potassium iodide solution according to Lugol following a previously published protocol.[62]

4.10. High-performance liquid chromatography (HPLC)

Chromatographic separations were performed on an UltiMate™ 3000 Rapid Separation (RS) Ultra-High-Performance Liquid Chromatography (UHPLC) system from Thermo Fisher Scientific (USA). A monolithic Chromolith® High Resolution RP-18 endcapped (100 × 4.6 mm) column from Merck KGaA was used as stationary phase. The column oven temperature was set to 30 °C for all measurements.

The elution behavior of the polymers was investigated using a gradient elution method. For that, the polymers, *i.e.*, **PLGA**, **Ac-Dex**, **PValG**, and **PPheG**, were dissolved in 50/50 DMSO/CH$_3$CN (%, v/v) at a concentration of 1 mg mL^{-1}. The binary mobile phase consisted of CH$_3$CN and H$_2$O. The mobile phase composition was kept constant at 50/50 (%, v/v) CH$_3$CN/H$_2$O for 1 min. Afterward, the CH$_3$CN content was increased to 100% within 10 min, followed by an isocratic hold at 100% CH$_3$CN for 8 min to enable the complete polymer elution from the column. Then, the initial conditions, *i.e.*, 50/50 (%, v/v) CH$_3$CN/H$_2$O were re-established within 1 min and the column was equilibrated for 5 min before the next injection. The autosampler temperature was set to 17 °C, the injection volume was 5 μL and a flow rate of 1.0 mL min^{-1} was utilized. The polymer elution was monitored using a universal charged aerosol detector (Corona™ Veo™ RS CAD, Thermo Fisher Scientific) with a data acquisition frequency of 5 Hz and an evaporator temperature of 45 °C.

To determine the amount of drug content in the **MF-15**- and **BRP-201**-loaded particles, the chromatographic system was operated with two detectors: a universal CAD to monitor the composition of **BRP-201**-loaded nanoparticles, and a selective diode array detector (DAD) operating at the respective API's (**MF-15** and **BRP-201**) absorbance maxima. The dissolved particles were analyzed based on a previously developed concept.[35]

For determination of **MF-15** content, the mobile phase consisted of CH$_3$CN and 0.1% (w/w) aqueous H$_3$PO$_4$. The lyophilized aliquots of **MF-15**-containing nanoparticles were dissolved in 500 μL DMSO, sonicated for 5 min at room temperature and further diluted with 500 μL 70/30 (%, v/v) CH$_3$CN/0.1% (w/w) aqueous H$_3$PO$_4$. The starting elution conditions were kept constant at 70/30 (%, v/v) CH$_3$CN/0.1% (w/w) H$_3$PO$_4$ for 3 min. After that, the CH$_3$CN content was increased to 100% within 0.25 min, followed by a 3.25 min isocratic hold. Afterward, the initial elution conditions, *i.e.*, 70% CH$_3$CN were re-established within 3.5 min and the column was equilibrated for 5 min before the next injection. The autosampler temperature was set to 15 °C and a flow rate of 1.0 mL min^{-1} was utilized. The elution of **MF-15** was monitored at 290 nm.

For determination of **BRP-201** content, the mobile phase consisted of CH$_3$CN and H$_2$O. Lyophilized aliquots of **BRP-201**-containing particles were dissolved in 200 μL DMSO, sonicated for 1 min at room temperature and were further diluted with 800 μL 85/15 (%, v/v) CH$_3$CN/H$_2$O. The starting elution conditions were kept constant at 85/15 CH$_3$CN/H$_2$O (%, v/v) for 4 min. The CH$_3$CN content was increased to 100% within 1 min, followed by a 3 min isocratic hold. Afterward, the initial elution conditions, *i.e.*, 85% CH$_3$CN were re-established within 0.5 min and the column was equilibrated for 2.5 min before the next injection. The autosampler temperature was set to 17 °C and a flow rate of 1.5 mL min^{-1} was utilized. The elution of **BRP-201** was monitored at 312 nm.

For establishing calibration curves, a 1 mg mL^{-1} stock solution of API, *i.e.*, **MF-15** or **BRP-201**, in DMSO was diluted to a series of concentrations, *e.g.*, 5 to 100 μg mL^{-1}. The calibration curves were established through plotting drug peak areas as a function of concentration (Fig. S13). The solvent composition in the calibration standards was the same as for the dissolved API-containing nanoparticle aliquots. For dissolved particle elution and drug calibration curves, an injection volume of 10 μL was used.

Prior to the analyses, all samples were filtered over a hydrophobic 0.45 μm pore size poly(tetrafluoroethylene) (PTFE) filter (AppliChrom, Germany). Chromatographic data were processed using the Thermo Scientific™ Dionex™ Chromeleon™ 7.2 SR5 Chromatography Data System software. The loading capacity (LC, in%) was calculated by dividing the mass of the drug determined by HPLC by the mass of lyophilized aliquot of nanoparticles multiplied by the factor of 100.

4.11. Cell isolation and cell culture

Leukocyte concentrates (provided by the University Hospital Jena, Germany) were prepared from peripheral blood of healthy adult human donors (males and females between age 18 to 65) who had not taken an anti-inflammatory medication in the previous ten days. The protocol was authorized by the University Hospital Jena's ethics committee, and all procedures followed the relevant rules and regulations, as outlined in an earlier standard protocol.[63,64] Leuconostoc spp. dextran was given to the leukocyte concentrates to separate erythrocytes. The supernatant was centrifuged on a lymphocyte separation medium (Histopaque®-1077, Sigma Aldrich, Missouri, USA) in order to separate neutrophils from peripheral blood mononuclear cells (PBMCs). Water-based hypotonic lysis eliminated remaining erythrocytes from the neutrophil fraction. After twice being cleaned in ice-cold phosphate-buffered saline (PBS) at pH 7.4, the pelleted neutrophils were resuspended in 5 mL of PBS. In order to isolate monocytes, PBMCs were seeded in cell culture flasks (Greiner Bio-One, Frickenhausen, Germany) with PBS pH 7.4 supplemented with CaCl$_2$ and MgCl$_2$ (Sigma-Aldrich, Steinheim, Germany). The medium was replaced by

15526 | *J. Mater. Chem. B*, 2025, **13**, 15516–15529

This journal is © The Royal Society of Chemistry 2025

RPM 1640 (Thermo Fisher Scientific, Schwerte, Germany) containing heat-inactivated fetal calf serum (FCS, 10% v/v), penicillin (100 U mL^{-1}), streptomycin (100 µg mL^{-1}), and L-glutamine (2 mmol L^{-1}) after 1 h at 37 °C and 5% CO_2 for monocyte adherence.

4.12. Macrophage differentiation and polarization

Differentiation of human monocytes to macrophages and subsequent polarization to M$_2$-like phenotypes were carried out as described previously.[65] In brief, freshly isolated PBMCs were cultured in RPMI 1640 supplemented with 10% FCS, L-glutamine, penicillin, and streptomycin for six days with 20 ng mL^{-1} M-CSF (Cell Guidance Systems Ltd, Cambridge, United Kingdom). The M0$_{M-CSF}$ MDMs were treated for 48 h with 20 ng mL^{-1} of IL-4 (PeproTech) to generate M$_2$-MDMs.

4.13. Determination of 5-LOX product formation in neutrophils

Human neutrophils were pre-incubated (5 × 10^6 in 1 mL) in PBS containing 0.1% glucose and 1 mM $CaCl_2$ with vehicle (PBS) and the nanoparticles (encapsulated with **BRP-201** at a concentration of 0.3 µM) for 15 min at 37 °C in order to assess the effects on 5-LOX product formation.[42] Ca^{2+}-ionophore A23187 (Cayman, Ann Arbor, USA) at a concentration of 2.5 µM was used to stimulate the cells for ten minutes. Following this, the incubation was halted using 1 mL of ice-cold methanol that contained 200 ng mL^{-1} prostaglandin B1. 5-LOX products were isolated by solid phase extraction and then separated and analyzed via RP-HPLC in accordance with an established protocol.[66]

4.14. Cell integrity analysis using LDH release assay

Lactate dehydrogenase (LDH) release was evaluated for cell integrity analysis using the CytoTox 96® Non-Radioactive Cytotoxicity test kit. After incubation of 1 × 10^6 M0$_{M-CSF}$, the supernatants were diluted to appropriate LDH concentrations and centrifuged at 400 g for 5 minutes at 4 °C. Triton X-100 was used as a positive control. To measure the absorbance at 490 nm, a NOVOstar microplate reader (BMG LABTECH GmbH, Offenburg, Germany) was utilized. The criteria provided by the manufacturer were followed in determining the cell integrity and data were normalized to positive control.

4.15. Incubation for lipid mediator (LM) formation and LM metabololipidomics by UPLC-MS-MS

To study the effects of the MF15 and MF15-loaded nanoparticles on LM formation, M2-MDM (1 × 10^6 mL^{-1} PBS containing 1 mM $CaCl_2$) were incubated with vehicle (PBS), **MF-15** (3 µM) or nanoparticles (3 µM) for 180 min at 37 °C and 5% CO_2. Afterward, the reaction was stopped by addition of 2 mL of ice-cold methanol containing deuterated LM standards (200 nM d8-5S-HETE, d4-LTB$_4$, d5-LXA$_4$, d5-RvD2, d4-PGE2 and 10 µM d8-AA; Cayman Chemical/Biomol GmbH, Hamburg, Germany). The samples were kept at −20 °C for at least 60 min to allow protein precipitation. The extraction of LM was performed as recently published.[44] In brief, after centrifugation (1200×g; 4 °C; 10 min), acidified H_2O (9 mL; final pH = 3.5) was added and samples were extracted on solid phase cartridges (Sep-Pak® Vac 6cc 500 mg/6 mL C18; Waters, Milford, MA, USA). After equilibration of the cartridges with methanol followed by H_2O the samples were washed using H_2O and then n-hexane. LM were eluted with methyl formate (6 mL). The solvent was fully evaporated using an evaporation system (TurboVap LV, Biotage, Uppsala, Sweden) and the residue was resuspended in 150 µL methanol/water (1 : 1, v/v) for UPLC-MS-MS analysis. LM were analyzed with an Acquity™ UPLC system (Waters, Milford, MA, USA) and a QTRAP 5500 Mass Spectrometer (ABSciex, Darmstadt, Germany) equipped with a Turbo V™ Source and electrospray ionization. LM were eluted using an ACQUITY UPLC® BEH C18 column (1.7 µm, 2.1 mm × 100 mm; Waters, Eschborn, Germany) at a column oven temperature of 50 °C, with a flow rate of 0.3 mL min^{-1}, and a mobile phase consisting of methanol–water–acetic acid at a ratio of 42 : 58 : 0.01 (%, v/v/v) that was ramped to 86 : 14 : 0.01 (v/v/v) over 12.5 min and then to 98 : 2 : 0.01 (%, v/v/v) for 3 min. The QTRAP 5500 was run in negative ionization mode using scheduled multiple reaction monitoring (MRM) coupled with information-dependent acquisition. The scheduled MRM window was 60 s, optimized LM parameters were adopted, with a curtain gas pressure of 35 psi. The retention time and at least six diagnostic ions for each LM were confirmed by means of an external standard for each and every LM (Cayman Chemical/Biomol GmbH). Quantification was achieved by calibration curves for each LM. Linear calibration curves were obtained for each LM and gave $r2$ values of 0.998 or higher. The limit of detection for each targeted LM was determined as described previously.[67] The identity of low abundance analytes was confirmed by fragmentation pattern matching by re-analysis using a QTrap 7500 mass spectrometer (Sciex, Framingham, MA, USA) controlled by SCIEX-OS, and comparing the enhanced product ion scans of the biological sample with that of authentic standards.

Conflicts of interest

The authors declare no competing financial interest.

Data availability

The data supporting this article have been included as part of the supplementary information (SI). The SI contains comprehensive details on polymer synthesis and characterization, formulation and characterization of nanoparticles, and HPLC measurement data. See DOI: **https://doi.org/10.1039/d5tb01949d**.

Acknowledgements

References

1 C. Englert, J. C. Brendel, T. C. Majdanski, T. Yildirim, S. Schubert, M. Gottschaldt, N. Windhab and U. S. Schubert, *Prog. Polym. Sci.*, 2018, **87**, 107–164.

2 E. M. Elmowafy, M. Tiboni and M. E. Soliman, *J. Pharm. Investig.*, 2019, **49**, 347–380.

3 F. Danhier, E. Ansorena, J. M. Silva, R. Coco, A. Le Breton and V. Préat, *J. Controlled Release*, 2012, **161**, 505–522.

4 K. Fu, D. W. Pack, A. M. Klibanov and R. Langer, *Pharm. Res.*, 2000, **17**, 100–106.

5 K. Fu, A. M. Klibanov and R. Langer, *Nat. Biotechnol.*, 2000, **18**, 24–25.

6 W. Alam, H. Khan, M. S. Jan, H. W. Darwish, M. Daglia and A. A. Elhenawy, *PLoS One*, 2024, **19**, e0297398.

7 A. Seifelnasr, M. Talaat, X. A. Si and J. Xi, *Curr. Pharm. Biotechnol.*, 2024, **25**, 787–798.

8 M. Behnke, P. Klemm, P. Dahlke, B. Shkodra, B. Beringer-Siemers, J. A. Czaplewska, S. Stumpf, P. M. Jordan, S. Schubert, S. Hoeppener, A. Vollrath, O. Werz and U. S. Schubert, *Int. J. Pharm.: X*, 2023, **5**, 100173.

9 M. Winnacker and B. Rieger, *Polym. Chem.*, 2016, **7**, 7039–7046.

10 T. Ouchi, M. Sasakawa, H. Arimura, M. Toyohara and Y. Ohya, *Polymer*, 2004, **45**, 1583–1589.

11 W. P. Ye, X. Yong and F. S. Du, *Pharm. Dev. Technol.*, 1999, **4**, 97–106.

12 D. Yamanouchi, J. Wu, A. N. Lazar, K. Craig Kent, C.-C. Chu and B. Liu, *Biomaterials*, 2008, **29**, 3269–3277.

13 Z. Li and L. Huang, *J. Controlled Release*, 2004, **98**, 437–446.

14 K. Guo and C. C. Chu, *J. Biomed. Mater. Res. B Appl. Biomater.*, 2009, **89B**, 491–500.

15 L. J. del Valle, D. Roca, L. Franco, J. Puiggalí and A. Rodríguez-Galán, *J. Appl. Polym. Sci.*, 2011, **122**, 1953–1967.

16 J. Zhang, L. Wang, M. Ding, X. You, J. Wu and J. Pang, *BME Front.*, 2023, **4**, 0025.

17 M. Behnke, A. Vollrath, P. Dahlke, F. P. Larios, M. Chi, E. Tsarenko, P. M. Jordan, C. Weber, M. Dirauf, J. A. Czaplewska, B. Beringer-Siemers, S. Stumpf, C. Kellner, C. Kretzer, S. Hoeppener, I. Nischang, M. Sierka, C. Eggeling, O. Werz and U. S. Schubert, *Mater. Today Chem.*, 2024, **35**, 101848.

18 A. Farber, T. W. Tan, D. Rybin, J. A. Kalish, N. M. Hamburg, G. Doros, P. P. Goodney and J. L. Cronenwett, *J. Vasc. Surg.*, 2013, **57**, 635–641.

19 S. Wang, F. Fontana, M.-A. Shahbazi and H. A. Santos, *Chem. Commun.*, 2021, **57**, 4212–4229.

20 C. Kretzer, B. Shkodra, P. Klemm, P. M. Jordan, D. Schröder, G. Cinar, A. Vollrath, S. Schubert, I. Nischang, S. Hoeppener, S. Stumpf, E. Banoglu, F. Gladigau, R. Bilancia, A. Rossi, C. Eggeling, U. Neugebauer, U. S. Schubert and O. Werz, *CMLS*, 2021, **79**, 40.

21 D. Liu, H. Zhang, E. Mäkilä, J. Fan, B. Herranz-Blanco, C.-F. Wang, R. Rosa, A. J. Ribeiro, J. Salonen, J. Hirvonen and H. A. Santos, *Biomaterials*, 2015, **39**, 249–259.

22 E. A. Torrico Guzmán, Q. Sun and S. A. Meenach, *ACS Biomater. Sci. Eng.*, 2019, **5**, 6570–6580.

23 F. Kong, H. Zhang, X. Zhang, D. Liu, D. Chen, W. Zhang, L. Zhang, H. A. Santos and M. Hai, *Adv. Funct. Mater.*, 2016, **26**, 6158–6169.

24 C. B. Braga, G. Perli, T. B. Becher and C. Ornelas, *Mol. Pharm.*, 2019, **16**, 2083–2094.

25 K. Mint, J. P. Morrow, N. M. Warne, X. He, D. Pizzi, S. Z. O. Shah, G. K. Pierens, N. L. Fletcher, C. A. Bell, K. J. Thurecht and K. Kempe, *Polym. Chem.*, 2024, **15**, 2662–2676.

26 E. Tsarenko, N. E. Göppert, P. Dahlke, M. Behnke, G. Gangapurwala, B. Beringer-Siemers, L. Jaepel, C. Kellner, D. Pretzel, J. A. Czaplewska, A. Vollrath, P. M. Jordan, C. Weber, O. Werz, U. S. Schubert and I. Nischang, *J. Mater. Chem. B*, 2024, **12**, 11926–11938.

27 M. Kötzsche, J. Egger, A. Dzierza, L. S. Reichel, I. Nischang, A. Traeger, D. Fischer and K. Peneva, *J. Mater. Chem. B*, 2025, **13**, 6066–6076.

28 D. J. Greenhalgh, A. C. Williams, P. Timmins and P. York, *J. Pharm. Sci.*, 1999, **88**, 1182–1190.

29 B. C. Hancock, P. York and R. C. Rowe, *Int. J. Pharm.*, 1997, **148**, 1–21.

30 I. Muljajew, M. Chi, A. Vollrath, C. Weber, B. Beringer-Siemers, S. Stumpf, S. Hoeppener, M. Sierka and U. S. Schubert, *Eur. Polym. J.*, 2021, **156**, 110606.

31 D. Pospiech, A. Gottwald, D. Jehnichen, P. Friedel, A. John, C. Harnisch, D. Voigt, G. Khimich and A. Y. Bilibin, *Colloid Polym. Sci.*, 2002, **280**, 1027–1037.

32 *ICH Q3C (R9) Guideline on impurities: guideline for residual solvents*, European Medicines Agency, Amsterdam, 2024, vol. 9, **https://www.ema.europa.eu/en/documents/scientific-guideline/ich-q3c-r9-guideline-impurities-guideline-residual-solvents-step-5_en.pdf**.

33 W. Huang and C. Zhang, *Biotechnol. J.*, 2018, **13**, 1700203.

34 Z. H. Mok, *Pharm. Sci. Adv.*, 2024, **2**, 100031.

35 E. Tsarenko, U. S. Schubert and I. Nischang, *Anal. Chem.*, 2023, **95**, 565–569.

36 G. Tiwari, R. Tiwari, B. Sriwastawa, L. Bhati, S. Pandey, P. Pandey and S. K. Bannerjee, *Int. J. Pharm. Investig.*, 2012, **2**, 2–11.

37 W. Abdelwahed, G. Degobert and H. Fessi, *Int. J. Pharm.*, 2006, **309**, 178–188.

38 N. Kamaly, B. Yameen, J. Wu and O. C. Farokhzad, *Chem. Rev.*, 2016, **116**, 2602–2663.

39 A. C. Fonseca, M. H. Gil and P. N. Simões, *Prog. Polym. Sci.*, 2014, **39**, 1291–1311.

15528 | *J. Mater. Chem. B*, 2025, **13**, 15516–15529

This journal is © The Royal Society of Chemistry 2025

40 P. Ranganathan, C.-W. Chen, S.-P. Rwei, Y.-H. Lee and S. K. Ramaraj, *Polym. Degrad. Stab.*, 2020, **181**, 109323.

41 P. J. Sweeney and J. M. Walker, in *Enzymes of Molecular Biology*, ed: M. M. Burrell, Humana Press, Totowa, NJ, 1993, pp. 305–311.

42 C. Kretzer, P. M. Jordan, R. Bilancia, A. Rossi, T. Gür Maz, E. Banoglu, U. S. Schubert and O. Werz, *J. Inflamm. Res.*, 2022, 911–925.

43 P. Dahlke, L. K. Peltner, P. M. Jordan and O. Werz, *Front. Pharmacol.*, 2023, **14**, 1219160.

44 C. Kretzer, P. M. Jordan, K. P. L. Meyer, D. Hoff, M. Werner, R. K. Hofstetter, A. Koeberle, A. Cala Peralta, G. Viault, D. Seraphin, P. Richomme, J.-J. Helesbeux, H. Stuppner, V. Temml, D. Schuster and O. Werz, *Biochem. Pharmacol.*, 2022, **195**, 114825.

45 O. Radmark, *Biochem. Pharmacol.*, 2022, **204**, 115210.

46 E. Banoglu, E. Çelikoğlu, S. Völker, A. Olgaç, J. Gerstmeier, U. Garscha, B. Çalışkan, U. S. Schubert, A. Carotti, A. Macchiarulo and O. Werz, *Eur. J. Med. Chem.*, 2016, **113**, 1–10.

47 D. Systèmes. (n.d.)*Materials Studio*. Retrieved January 14, 2025, from **https://www.3ds.com/products/biovia/materials-studio.**

48 R. L. C. Akkermans, N. A. Spenley and S. H. Robertson, *Mol. Simul.*, 2021, **47**, 540–551.

49 D. N. Theodorou and U. W. Suter, *Macromolecules*, 1985, **18**, 1467–1478.

50 S. Nosé, *J. Chem. Phys.*, 1984, **81**, 511–519.

51 W. G. Hoover, *Phys. Rev. A: At., Mol., Opt. Phys.*, 1985, **31**, 1695–1697.

52 H. J. C. Berendsen, J. P. M. Postma, W. F. van Gunsteren, A. DiNola and J. R. Haak, *J. Chem. Phys.*, 1984, **81**, 3684–3690.

53 M. Parrinello and A. Rahman, *Phys. Rev. Lett.*, 1980, **45**, 1196–1199.

54 P. J. Flory, *J. Chem. Phys.*, 1942, **10**, 51–61.

55 M. L. Huggins, *J. Am. Chem. Soc.*, 1942, **64**, 1712–1719.

56 L. Huynh, J. Grant, J.-C. Leroux, P. Delmas and C. Allen, *Pharm. Res.*, 2008, **25**, 147–157.

57 M. Rubinstein and R. H. Colby, *Polymer Physics*, Oxford University Press, 2003.

58 W. Hu, *Polymer physics: a molecular approach*, Springer Science & Business Media, 2012.

59 D. Merino-Garcia and S. Correra, *J. Dispers. Sci. Technol.*, 2007, **28**, 339–347.

60 A. Erlebach, I. Muljajew, M. Chi, C. Bückmann, C. Weber, U. S. Schubert and M. Sierka, *Adv. Theory Simul.*, 2020, **3**, 2000001.

61 M. Chi, R. Gargouri, T. Schrader, K. Damak, R. Maâlej and M. Sierka, *Polymers*, 2022, **14**, 26.

62 S. Spek, M. Haeuser, M. M. Schaefer and K. Langer, *Appl. Surf. Sci.*, 2015, **347**, 378–385.

63 P. M. Jordan, J. Gerstmeier, S. Pace, R. Bilancia, Z. Rao, F. Börner, L. Miek, Ó. Gutiérrez-Gutiérrez, V. Arakandy and A. Rossi, *Cell Rep.*, 2020, 33.

64 K. Günther, C. Ehrhardt, O. Werz and P. M. Jordan, *STAR Protoc*, 2024, **5**, 103142.

65 O. Werz, J. Gerstmeier, S. Libreros, X. De la Rosa, M. Werner, P. C. Norris, N. Chiang and C. N. Serhan, *Nat. Commun.*, 2018, **9**, 59.

66 O. Werz, E. Bürkert, B. Samuelsson, O. Rådmark and D. Steinhilber, *Blood*, 2002, **99**, 1044–1052.

67 M. Werner, P. M. Jordan, E. Romp, A. Czapka, Z. Rao, C. Kretzer, A. Koeberle, U. Garscha, S. Pace and H.-E. Claesson, *FASEB J.*, 2019, **33**, 6140.

This journal is © The Royal Society of Chemistry 2025

J. Mater. Chem. B, 2025, **13**, 15516–15529 | **15529**